Hybrid shallow on-axis and deep off-axis hydrothermal circulation at fast spreading ridges

Jörg Hasenclever[a*], Sonja Theissen-Krah[b], Lars H. Rüpke[a], Jason P. Morgan[c], Karthik Iyer[a], Sven Petersen[a], Colin W. Devey[a]

[a]GEOMAR, Helmholtz Centre for Ocean Research Kiel, Wischhofstraße 1-3, 24148 Kiel, Germany

[b]Department of Geosciences and Centre for Earth Evolution and Dynamics (CEED), University of Oslo, PO Box 1048, Blindern, 0316 Oslo, Norway

[c]Department of Earth Sciences, Royal Holloway, University of London, Egham, Surrey TW20 0EX, UK

[*]Corresponding author

Hydrothermal flow at oceanic spreading centres accounts for about ten per cent of all heat flux in the oceans[1,2] and controls the thermal structure of young oceanic plates. It also influences ocean and crustal chemistry, provides a basis for chemosynthetic ecosystems, and has formed massive sulphide ore deposits throughout Earth´s history. Despite this, how and under what conditions heat is extracted, in particular from the lower crust, remains largely unclear. Here we present high-resolution, whole-crust, two- and three-dimensional simulations of hydrothermal flow beneath fast spreading ridges that predict the existence of two interacting flow components, controlled by different physical mechanisms, that merge above the melt lens to feed ridge-centred vent sites. Shallow on-axis flow structures develop owing to the thermodynamic properties of water, whereas

deeper off-axis flow is strongly shaped by crustal permeability, particularly the brittle–ductile transition. About 60 per cent of the discharging fluid mass is replenished on-axis by warm (up to 300 degrees Celsius) recharge flow surrounding the hot thermal plumes, and the remaining 40 per cent or so occurs as colder and broader recharge up to several kilometres away from the axis that feeds hot (500-700 degrees Celsius) deep-rooted off-axis flow towards the ridge. Despite its lower contribution to the total mass flux, this deep off-axis flow carries ~70 per cent of the thermal energy released at the ridge axis. This combination of two flow components explains the seismically determined thermal structure of the crust and reconcile previously incompatible models favouring either shallower on-axis[3-5] or deeper off-axis hydrothermal circulation[6-8].

The fast-spreading East Pacific Rise (EPR) at 9° N is one of the best-studied ridge sections worldwide. Multichannel seismic studies between 9° N and 13° N image a nearly continuous sub-axial melt lens at depths of about 1.2-2.4 km (ref. 9). A tomographic study[10] at 9° 30’ N shows a narrow P-wave anomaly below the melt lens that is best modelled as a 4-5-km-wide, high temperature region extending through the whole crust and only widening at depths below the crust-mantle boundary (Fig. 1a). Isotherms are steep near this ‘hot slot’ but become nearly horizontal further off-axis, consistent with field observations from the Oman ophiolite[7,11]. Axis-perpendicular two-dimensional (2D) hydrothermal flow models[12,13] show that this implies hydrothermal convection through the entire crust[14], with hydrothermal fluids probably migrating parallel to the steep isotherms and thereby altering the lower gabbros at some distance away from the ridge axis[15]. This is in contrast to the conclusion, drawn from microearthquake distributions[5] at EPR 9° N, that hydrothermal cells develop

predominantly above the melt lens—a concept apparently supported by vent fluid chemistry studies[16] and previous three-dimensional (3D) simulations of hydrothermal flow at fast-spreading ridges[4,17].

To investigate how whole-crustal cooling can be reconciled with supra-melt lens fluid circulation, we developed a 3D model that resolves hydrothermal flow throughout the entire thickness of the oceanic crust at a fast-spreading ridge. We obtain the permeability structure for this 3D model from 2D numerical experiments in which we simultaneously solve for crustal accretion processes and cooling by hydrothermal flow[18]. This 2D model predicts the thermal structure of the young crust and the depth of the melt lens for a given permeability field and a full spreading rate of 11 cm yr^{-1} (see ref. 18 and Methods). Permeability decreases exponentially with depth and linearly with distance from the ridge axis and was varied until (1) the predicted crustal temperature field matches the one inferred from seismic tomography[10] and (2) the melt lens (corresponding to the 1200 °C isotherm) is located at the observed depth[9] of 1400 m. Key features of this parameterized permeability field (see Methods and Extended Data Fig. 1) are relatively high permeabilities adjacent to the margins of the 'hot slot', mimicking the effects of a thermal cracking front[19]. This is consistent with microcracks found in lower gabbros[7] and in peridotites a few hundred meters below the crust-mantle boundary[20] of the Oman ophiolite. An additional decrease in permeability beyond a distance to the ridge of 5 km is required to reproduce the seismically inferred nearly horizontal isotherms[10] in this region and to be consistent with the low permeabilities inferred from porosity logs from drill holes in more mature oceanic crust[21]. The brittle–ductile transition in the lower crust[22] is accounted for by decreasing permeability to 10^{-18} m^2 between 600°C and 800°C, so that no significant fluid flow

occurs through rock hotter than 800°C. The top of the model has a 250-m-thick pillow basalt layer[23] in which permeability increases to 10^{-13} m^2 at the seafloor.

The 2D results (Fig. 1b) show the thermal evolution of the oceanic crust after 500,000 years of simulation time in response to the interplay of crustal accretion processes and hydrothermal cooling. The hydrothermal flow patterns predicted by the 2D model (Fig. 1c) hint at two coexisting flow components: (1) on-axis convection above the melt lens with strong adjacent recharge flow and (2) much broader and deeper off-axis circulation. Both flow components merge above the melt lens and supply the axial discharge.

Using a 3D hydrothermal flow model (see Methods) we constrain the relative importance of on- versus off-axis flow and explore the detailed flow structures developing over shorter timescales of a few thousand years. Whereas previous 3D[4,17] and across-axis 2D[12,13,18] models had focused either on supra-melt lens or ridge-perpendicular flow, we use a whole-crust 3D finite-element model that resolves both flow components simultaneously. Fluid properties are determined from the pure water IAPS-84 equation of state, so that the fluid is in the supercritical single-phase regime for the hydrostatic pressures prevailing at the seafloor. The 1000°C isotherm derived from the 2D results at steady state is used as a constant-temperature lower boundary for the 3D domain, whereas the top boundary follows a smoothed-average bathymetry of the EPR at 9°N. Fluids are free to enter (at 2˚C temperature) or to leave the domain through the top boundary only. Sidewalls are impermeable and insulating. This set-up results in a 16km x 6 km x 6.5 km-sized computational domain that is meshed with about 25 million tetrahedral elements (Extended Data Fig. 2). Each 3D simulation ran on a cluster with 32 processors for about 3 weeks.

Our 3D results show the formation of a single hybrid hydrothermal system (Fig. 1d, e). On-axis upflow organizes into a network of closely interconnected thermal plumes that feed high-temperature (up to 410˚C) axial vent fields with an along-axis spacing between 500 and 1,000 m. Partial 'on-axis' recharge surrounds the thermal plumes and does not penetrate deeper than the depth of the melt lens (see Fig. 1e), consistent with earlier findings by ref. 4. In contrast, 'off-axis' recharge flow occurs over a broad area and feeds very hot (500-700˚C) ridge-perpendicular flow upslope the flanks of the hot slot, showing no significant ridge-parallel motion until the melt lens depth is reached, where the fluid starts to focus into tubes with a spacing similar to that of the on-axis plumes (Fig. 1d,e). Near the top of the melt lens both flow components merge before feeding the axial vent fields, where fluids are released at a rate of 80-90 kg s^{-1} per kilometre ridge axis. A quantification of the fluid mass fluxes as a function of distance to the ridge (Fig. 2a) shows that, on average, about 60% of the entire recharge flow occurs on-axis (within 1.1 km to the ridge axis), while about 40% of the venting fluids originate from distances greater than 1.1 km. This ratio also holds for simulations with along-ridge variations in melt lens depth (see Extended Data Figs 4 and 5).

An analysis of vertical mass fluxes versus temperature (Fig. 2b and Extended Data Fig. 3) reveals that fundamentally different processes shape on-axis (red bars) and off-axis (blue bars) flow. On-axis, most upflow occurs at 300-450 ˚C, whereas downflow is strongest between 100-200 ˚C. These preferred temperature ranges are controlled by the thermodynamic properties of water[4,24]. Upflow occurs at temperatures around 425°C, at which (for the prevailing pressures) the ability of water to transport energy by buoyancy-driven flow (that is, the fluid's 'fluxibility'[24]) is maximum. This also explains

why even hotter fluids remain at depth and do not directly feed the on-axis plumes (see Fig. 1d and 2c). Extending the fluxibility concept to predict most efficient recharge flow[4] yields temperatures between 100 ˚C and 200 ˚C, which is where we also identify strongest on-axis recharge flow (Fig. 2b). The energy required to heat the recharge flow is provided by the rising plumes, explaining why recharge is strongest adjacent to hot plumes (see Fig. 2c). The mass flux distribution for the off-axis flow component (blue bars in Fig. 2b) differs significantly, with upward mass flux extending to much higher temperatures and most recharge flow occurring at colder temperatures. This implies that factors in addition to the fluid's fluxibility also control the deeper flow. Almost half of off-axis recharge flow occurs below 50 ˚C simply because no off-axis thermal plumes are present to heat the recharge. The extensive area of pervasive off-axis recharge compensates for these thermodynamically inefficient cold conditions. Upflow within the lower crust occurs over a broader range of higher temperatures and decreases towards 700 ˚C because permeability is reduced at the brittle–ductile transition (Fig. 2b, Extended Data Fig. 1). Hence, the off-axis upflow along the flanks of the hot slot is predominantly shaped by the crustal permeability structure, whereas the on-axis circulation forms thermal plumes more strongly controlled by the thermodynamic properties of water.

Pressure–temperature paths of numerical fluid tracers (Fig. 3) further highlight the characteristics of on-axis (red paths) and off-axis (blue paths) fluid circulation. With fluxibility limiting the temperatures in rising plumes above the melt lens to values below about 450 °C, the hot (up to 700 °C) deep-rooted fluids migrating towards the top of the melt lens cannot rise further until they cool below about 450˚C by mixing with the on-axis component. This may explain why maximum pressures of last fluid-rock

equilibration correlate very well with the depth of the axial melt lens[16], even though a significant mass fraction of the venting fluids may actually have migrated through much deeper and hotter parts of the oceanic crust prior to venting. The pressure-temperature paths of on- and off-axis components also resolve an apparent discrepancy between *in situ* measurements of vent temperatures at the EPR and temperatures of hydrothermal circulation estimated from fluid inclusions in gabbros from the Oman ophiolite[25] and the extinct Mathematician Ridge[26] (Fig. 3). Despite the clear upper limit in observed axial vent temperatures[27], fluid inclusion data show much higher entrapment temperatures that are strikingly consistent with the temperatures our 3D model predicts for most deep off-axis upflow.

Our simulations have a total hydrothermal energy flux of about 9 x 10^7 Watt per kilometre ridge axis, which is in excellent agreement with estimates for the total magmatic energy input[28] at a ridge with a full spreading rate of 11 cm yr^{-1}. The model allows us to quantify the energy fluxes from upper and lower crust into the ocean. Despite contributing only 40% to the total fluid mass flux, the 500 ˚C–700 ˚C upflow in the lower crust transports about 70% of the total energy released at the hydrothermal vent sites because it carries more thermal energy per kg fluid than the <450 °C hot thermal plumes above the melt lens. This implies that not only is heat efficiently mined from the lower crust, but also that deep off-axis circulation may be the dominant process that cools the oceanic crust. Furthermore, the relative contributions of on- and off-axis hydrothermal flow to the total energy flux from crust to ocean are linked to the depth of the axial melt lens, where the transition in flow structure from hot (mainly permeability-controlled) flow in the lower gabbros to cooler (mainly fluid property-controlled) flow in plumes occurs.

This new hybrid hydrothermal flow structure reconciles previously incompatible observations and models that suggested either strong on-axis[4,5] or deeper ridge-perpendicular hydrothermal circulation[6,10,15]. We find both modes exist and naturally merge into a single hybrid flow structure in our whole-crust numerical experiments. The on-axis flow component is more vigorous and contributes slightly more to the total mass flux. It controls the depth of the melt lens and explains why high-temperature vent systems associated with fast-spreading ridges have so far been observed only directly on-axis. The deeper off-axis flow component provides about 70% of the hydrothermal energy flux and is what makes the overall thermal structure of the young oceanic crust consistent with seismic tomography data[10] and the pervasive crustal-scale hydrothermal convection inferred from *in situ* analysis of the Oman ophiolite[7,15]. This implies that the entire oceanic crust experiences extensive high-temperature hydrothermal circulation, providing a mechanism to scavenge elements from the lower crust. Recent mass balance calculations reveal that the amounts of metal potentially mobilized by hydrothermal flow at ridges[12] are far greater than estimates based on the size of known ridge-linked massive sulphide deposits[29]. Our simulations predict a cooling of about 200 ˚C of deeper off-axis fluids upon mixing with the on-axis component above the melt lens, which would lead to strong precipitation of dissolved metals near the roots of the sheeted dykes. Entrainment of cold sea water is likely to result in further re-deposition of metal within the pillow basalt layer. Finally, chemical differences between individual vents of the same vent field as observed at the neighbouring P and Bio9 vents[30] at EPR 9°50'N could result from mixing processes between fluids that obtained distinct chemical signatures while cycling through the conjoined limbs of a single hybrid hydrothermal system.

Methods Summary

We constructed a 2D numerical model[18] representing a vertical cross-section perpendicular to a fast spreading ridge to solve for the long-term thermal evolution of oceanic crust and mantle. Hydrothermal convection of pure water is coupled to crustal accretion by the temperature field. Fluid flow is treated as Darcy flow through a porous medium with parameterized permeability, and we solve for temperature, pore pressure and fluid velocity using an implicit finite element method. Deformation of the crust is formulated as viscous creep of an incompressible medium and a dilation term is used to simulate crustal accretion in melt lens and dyking region. 2D simulations ran until a quasi-steady state was reached, typically after 200,000–500,000 years. The purpose of this model is to define a permeability field which leads to a thermal structure matching that inferred from seismic data[10]. Furthermore, the melt lens (corresponding to the 1,200 ˚C isotherm) should be located at the observed depth of 1,400 m. The obtained permeability field forms the basis for the 3D model, which covers the crustal volume above the 1,000 ˚C isotherm in the 2D results and extends 6 km along the ridge and 8 km to each side of the ridge. In- and outflow are allowed through the top boundary only. The numerical formulation of hydrothermal flow is very similar to that used in the 2D model, but solving the much larger system of equations required parallelization of the 3D model and iterative solution algorithms[31]. Each 3D calculation starts at cold crustal conditions, with the exception of a hot boundary layer along the bottom boundary that forms after 300 years of purely conductive heating before model initiation. Each 3D calculation simulated 2,000–8,000 years, after which vent field locations stabilized and discharging mass fluxes became nearly constant.

References:

1. Stein, C. A. & Stein, S. Constraints on hydrothermal heat flux through the oceanic lithosphere from global heat flow. *J. Geophys. Res.* **99,** 3081–3095 (1994).
2. Baker, E., Chen, Y. & Phipps Morgan, J. The relationship between near-axis hydrothermal cooling and the spreading rate of mid-ocean ridges. *Earth Planet. Sci. Lett.* **142,** 137–145 (1996).
3. Singhal, B. B. S. & Gupta, R. P. *Applied Hydrogeology of Fractured rocks*. (Kluwer Academic, 1999).
4. Coumou, D., Driesner, T. & Heinrich, C. A. The structure and dynamics of mid-ocean ridge hydrothermal systems. *Science* **321,** 1825–1828 (2008).
5. Tolstoy, M., Waldhauser, F., Bohnenstiehl, D. R., Weekly, R. T. & Kim, W. Y. Seismic identification of along-axis hydrothermal flow on the East Pacific Rise. *Nature* **451,** 181–184 (2008).
6. Cathles, L. M. A capless 350 ˚C flow zone model to explain megaplumes, salinity variations, and high-temperature veins in ridge axis hydrothermal systems. *Econ. Geol.* **88,** 1977–1988 (1993).
7. Nicolas, A., Mainprice, D. & Boudier, F. High-temperature seawater circulation throughout crust of oceanic ridges: a model derived from the Oman ophiolites. *J. Geophys. Res.* **108** (B8), 2371, http://dx.doi.org/10.1029/2002JB002094 (2003).
8. Johnson, H. P., Becker, K. & Von Herzen, R. Near-axis heat flow measurements on the northern Juan De Fuca Ridge: implications for fluid circulation in oceanic crust. *Geophys. Res. Lett.* **20,** 1875–1878 (1993).
9. Detrick, R. S. *et al.* Multi-channel seismic imaging of a crustal magma chamber along the East Pacific Rise. *Nature* **326,** 35–41 (1987).
10. Dunn, R. A., Toomey, D. R. & Solomon, S. C. Three-dimensional seismic structure

and physical properties of the crust and shallow mantle beneath the East Pacific Rise at 9° 30'N. *J. Geophys. Res.* **105,** 23537–23555 (2000).

11. VanTongeren, J. A., Kelemen, P. B. & Hanghøj, K. Cooling rates in the lower crust of the Oman ophiolite: Ca in olivine, revisited. *Earth Planet. Sci. Lett.* **267,** 69–82 (2008).
12. Cathles, L. M. What processes at mid-ocean ridges tell us about volcanogenic massive sulfide deposits. *Mineral. Dep.* **46,** 639–657 (2011).
13. Cherkaoui, A. S. M., Wilcock, W. S. D., Dunn, R. A. & Toomey, D. R. A numerical model of hydrothermal cooling and crustal accretion at a fast spreading mid-ocean ridge. *Geochem. Geophy. Geosyst.* **4,** 8616, http://dx.doi.org/10.1029/2001GC000215 (2003).
14. Fisher, A. T. in *Dahlem Workshop Report: Energy and Mass Transfer in Marine Hydrothermal Systems* (eds Halbach, P. E., Tunnicliffe, V. & Hein, J. R.) 29–52 (Dahlem Univ. Press, 2003).
15. Bosch, D. *et al.* Deep and high-temperature hydrothermal circulation in the Oman ophiolite—petrological and isotopic evidence. *Journal of Petrology* **45,** 1181–1208 (2004).
16. Fontaine, F. J., Wilcock, W. S. D., Foustoukos, D. E. & Butterfield, D. A. A Si-Cl geothermobarometer for the reaction zone of high-temperature, basaltic-hosted mid-ocean ridge hydrothermal systems. *Geochem. Geophy. Geosyst.* **10,** Q05009 (2009).
17. Coumou, D., Driesner, T., Geiger, S. & Paluszny, A. High-resolution three-dimensional simulations of mid-ocean ridge hydrothermal systems. *J. Geophys. Res.* **114,** B07104 (2009).
18. Theissen-Krah, S., Iyer, K., Rüpke, L. H. & Morgan, J. P. Coupled mechanical and

hydrothermal modeling of crustal accretion at intermediate to fast spreading ridges. *Earth Planet. Sci. Lett.* **311,** 275–286 (2011).

19. Lister, C. R. B. On the penetration of water into hot rock. *Geophys. J. R. Astron. Soc.* **39,** 465–509 (1974).

20. Boudier, F., Nicolas, A. & Mainprice, D. Does anisotropy of thermal contraction control hydrothermal circulation at the Moho level below fast spreading oceanic ridges? *Int. Geol. Rev.* **47,** 101–112 (2005).

21. Carlson, R. L. The effect of hydrothermal alteration on the seismic structure of the upper oceanic crust: evidence from Holes 504B and 1256D. *Geochem. Geophy. Geosyst.* **12,** Q09013 (2011).

22. Hirth, G., Escartin, J. & Lin, J. in *Faulting and Magmatism at Mid-Ocean Ridges* (eds Buck, W. R., Delaney, P. T., Karson, J. A.& Lagabrielle, Y.) **106**, 291–303 (American Geophysical Union, 1998).

23. Harding, A. J., Kent, G. M. & Orcutt, J. A. A multichannel seismic investigation of upper crustal structure at 9°N on the East Pacific Rise: implications for crustal accretion. *J. Geophys. Res.* **98,** 13925–13944 (1993).

24. Jupp, T. & Schultz, A. A thermodynamic explanation for black smoker temperatures. *Nature* **403,** 880–883 (2000).

25. Nehlig, P. Interactions between magma chambers and hydrothermal systems: oceanic and ophiolitic constraints. *J. Geophys. Res.* **98,** 19621–19633 (1993).

26. Vanko, D. A. Temperature, pressure, and composition of hydrothermal fluids, with their bearing on the magnitude of tectonic uplift at mid-ocean ridges, inferred from fluid inclusions in oceanic layer 3 rocks. *J. Geophys. Res.* **93,** 4595–4611 (1988).

27. Hannington, M. D., de Ronde, C. E. J. & Petersen, S. Sea-floor tectonics and

submarine hydrothermal systems. *Econ. Geol.* **100th Anniversary Volume,** 111–141 (2005).

28. Sinha, M. C. & Evans, R. L. in *Mid-Ocean Ridges: Hydrothermal Interactions Between the Lithosphere and Oceans* (eds German, C., Lin, J. & Parson, L.) **148,** 19–62 (American Geophysical Union, 2004).
29. Hannington, M., Jamieson, J., Monecke, T., Petersen, S. & Beaulieu, S. The abundance of seafloor massive sulfide deposits. *Geology* **39,** 1155–1158 (2011).
30. Fornari, D. *et al.* The East Pacific Rise between 9°N and 10°N: twenty-five years of integrated, multidisciplinary oceanic spreading center studies. *Oceanography* **25,** 18–43 (2012).
31. Hasenclever, J. *Modeling Mantle Flow and Melting Processes at Mid-Ocean Ridges and Subduction Zones—Development and Application of Numerical Models.* PhD thesis, Hamburg Univ. (2010).

Acknowledgements

We thank reviewers T. Driesner and P. Johnson for comments that led to more insights into hydrothermal energy transport and improved the manuscript.

Author contribution audit

J.H. and J.P.M. developed the 3D numerical model. J.H. carried out the 3D simulations, did the post-processing and designed the figures. 2D simulations were done by S.T.-K. and J.H. (using the 2D model developed by S.T.-K., L.H.R., K.I. and J.P.M.). J.H. and L.H.R. wrote the initial manuscript, to which J.P.M., S.T.-K., K.I., S.P. and C.W.D. contributed geological and thermodynamic implications. Figures and text were edited and improved by all

authors. All authors discussed the results and implications at all stages of the manuscript.

Figure captions

Figure 1: Results of our 2D and 3D numerical experiments. a, Seismic and inferred thermal structure beneath the EPR (re-drawn after plate 1 and figure 10 in ref. 10). b, Quasi-steady-state temperature field of a best-fitting 2D simulation using our coupled crustal accretion/solid flow (green streamlines) and hydrothermal convection (black streamlines) model. The permeability field is shown as white contours. c, Vertical fluid mass flux shows transient narrow on-axis and steady broad off-axis circulation; positive values correspond to upward fluid flow. d, Our 3D model resolves hydrothermal convection in a 6-km long and 16-km-wide modelling domain above the 1,000 ˚C isotherm (black bottom surface) obtained from the 2D results. Thermal evolution and vent field locations are shown after 3,500 years of simulation time. e, Flow paths of fluid tracers, colour-coded for temperature in a subsection of the 3D domain.

Figure 2: Mass flux analysis. a, Vertical mass flux of discharging and recharging fluid flow, evaluated 300 m below the sea floor, as a function of distance to the ridge axis. All fluid discharge, but only ~60% of recharge, occurs within a distance of 1.1 km of the ridge axis. The remaining ~40% recharge comes from fluids infiltrating the crust at greater distances. b, Vertical mass flux as a function of fluid temperature for on-axis (red) and off-axis (blue) flow components. Regions within the highly permeable pillow basalt layer and near the top of the melt lens have been excluded for clarification (see Extended Data Fig. 3). Percentage values are with respect to total upflow and downflow

within the entire domain, respectively. c, Vertical fluid mass flux shows on-axis thermal plumes at temperatures below ~450 ˚C that are surrounded by strong recharge flow (dark blue) at temperatures above 100 ˚C—both effects are consequences of pressure- and temperature-dependent fluid properties[4,24].

Figure 3: Comparison between observed and modelled hydrothermal fluid temperatures. In situ measurements of exit temperatures at EPR vents (see Methods) show a preferred range of 300 ˚C–400 ˚C. Temperature estimates based on fluid inclusions in gabbros from the Oman ophiolite[25] and the extinct Mathematician Ridge[26] (MR) are significantly higher. The pressure–temperature paths of on-axis (red) and off-axis (blue) fluid tracers in our 3D model explain the discrepancy. Highlighted paths 1 and 2 show warm recharge flow before ascending in plumes at temperatures below ~450 ˚C. In contrast, off-axis recharge flow (paths 3 and 4) is cold until reaching the steep thermal gradients at depth. Most of the subsequent upward flow occurs at 500 ˚C–700 ˚C—the temperature range suggested by fluid inclusion data. Fluid properties at these high temperatures are thermodynamically inefficient for plume formation[24] and off-axis fluids must cool by mixing with the on-axis component before they are able to feed a plume. Path 5 shows entrainment of cold sea water into a thermal plume within the pillow basalt layer. Dashed lines mark phase regions of sea water for orientation (L, liquid; V, vapour; H, halite) and CP marks the critical point of sea water.

Methods

General modelling setup. We use a 2D model for the long-term thermal evolution of oceanic crust and mantle (up to 40 km off-axis and down to 20 km depth) and a 3D model to focus on the hydrothermal flow structures evolving in the oceanic crust near

the ridge axis (slightly deeper than the brittle–ductile transition and up to 8 km off-axis on both sides of the ridge axis). The 2D model represents a vertical cross-section perpendicular to a fast spreading ridge with a full spreading rate of 11 cm yr^{-1}. Here we coupled a model for hydrothermal convection of pure water and a model for crustal accretion[18]. The main purpose of this model is to simulate the formation and thermal evolution of the young oceanic crust over several hundred thousand years. The nearly continuous melt lens with very little depth variation[9] along the ridge axis allows us to use this 2D approach. A key input parameter is the crustal permeability field, which strongly controls the hydrothermal convection patterns and thus the thermal evolution. Permeability is parameterized as an exponential function of depth and a linear function of distance to the ridge axis. We performed more than one hundred 2D simulations in which we iteratively refined the permeability field until thermal structures evolved that simultaneously matched (1) those inferred from seismic tomographic studies[10] and (2) predicted the melt lens (defined by the axial 1,200 ˚C isotherm) at a the observed depth[9] of 1,400 m. We ran all 2D calculations until a quasi-steady state was reached, at which the 800 ˚C, 1,000 ˚C and 1,200 ˚C isotherms kept their shapes. This state was typically achieved after 200,000–500,000 years of simulation time. Above the melt lens, vigorous hydrothermal convection with episodic plumes still persisted after this time (see Fig. 1c), however, this caused perturbations only at lower temperatures (<500 ˚C) and did not affect the overall thermal structure of the crust. The 2D results allowed us to identify the brittle part of the crust through which hydrothermal fluids are able to migrate. Ductile deformation of crustal rocks at higher temperatures[22] closes fractures, a process we account for by reducing the permeability between 600 ˚C and 800 ˚C. Consequently, hydrothermal flow is limited to temperatures below 800 ˚C (Fig. 1c). The second numerical tool is a 3D hydrothermal convection model whose purpose is to study the 3D

hydrothermal flow patterns that evolve in the oceanic crust using the permeability field obtained from 2D modelling. Here we focus on the transient flow patterns that develop in the brittle part of the crust over shorter timescales comparable to typical lifetimes of hydrothermal vent fields (thousands of years as opposed to hundreds of thousands of years).

The 2D model. The 2D numerical model is identical to the one presented by ref. 18. It consists of a hydrothermal part that describes Darcy flow of pure water through a porous medium and a mechanical part to model crustal accretion as well as viscous flow of crust and underlying mantle. Coupling between the two parts occurs through the temperature field in that hydrothermal convection cools the crust while magma injection, latent heat of crystallization and heat conduction from mantle into the crust increase the temperature. The water depth at the EPR yields pressures at the sea floor that are above the critical point of water so that the fluid will remain in the single-phase region. This allows us to use a temperature formulation for the energy equation, which is decoupled from the pressure equation by operator splitting. A fully implicit finite-element method is used to solve the pressure equation, the diffusive part of the energy equation, and to derive the Darcy velocities. Advection is modelled using a semi-Lagrange scheme, with a second–order accurate predictor–corrector method to integrate along trajectories, and element shape functions are used to interpolate properties at the origin point. We use unstructured meshes composed of triangular elements with quadratic–order shape functions. Pre-calculated look-up tables (computed using the program PROST[32]) based on the IAPS-84 formulation, defined by the International Association for the Properties of Water and Steam (IAPS), provide the fluid properties as functions of temperature and pressure. The second part of the model simulates the formation of oceanic crust at the spreading axis. Crust and mantle are

described as Boussinesq fluids that deform viscously (that is, Stokes flow). Incompressibility is assumed everywhere except in the melt lens and a region of dyke intrusion, where magma injection is accounted for using a dilation term. A penalty method in an iterative Uzawa-like form[33,34] is used in combination with triangular Crouzeix–Raviart elements (quadratic–order 7-node velocity and discontinuous linear 3-node pressure shape functions). The above methods have been implemented in a modified version of the MATLAB (http://www.mathworks.com) code MILAMIN[33]. All matrix equations are solved using the Cholesky direct solver of the numerical library SuiteSparse[35] (http://www.cise.ufl.edu/research/sparse/SuiteSparse). Our model setup assumes the gabbro glacier hypothesis[36,37] for crustal accretion, in which the lower crust crystallizes in an axial melt lens while the upper crust is formed in a dyking region above the melt lens. The geometry of this crustal accretion region is prescribed in our model in that the widths of the dyking region and the melt lens are fixed at 400 m and 1,200 m, respectively. However, the model is dynamic in that the depth of the melt lens is linked to the sub-axial depth of the 1,200 ˚C isotherm. This depth is evaluated at every time step and a new finite-element mesh is generated during the simulations using the software 'Triangle'[38] whenever the melt lens depth changes. Coupling between viscous and hydrothermal flow is restricted to the temperature field and associated feedbacks: cooling by hydrothermal convection affects the viscous deformation of the rocks and the depth of the axial melt lens, whereas heat input from mantle, magma injection and melt crystallization define where the brittle–ductile transition occurs, and hence the region where fluids are able to migrate through the rocks and transport thermal energy. At quasi-steady state a balance between conductive plus hydrothermal cooling and heat generation/conduction is established.

The crustal permeability field. The crustal permeability field is parameterized as a function of both depth z and distance x to the ridge axis. We account for the closure of pore space at the brittle–ductile transition by reducing permeability K to a minimum value of 10^{-18} m^2 between 600 ˚C and 800 ˚C. As a consequence, no significant hydrothermal flow occurs above 800 ˚C (see Fig. 1c) and temperature evolution above this temperature is controlled by heat conduction only. The permeability field (Extended Data Fig. 1) that results in a best-fitting thermal structure of the young crust is constructed by

$$K = b \cdot K_R \cdot \exp(a \cdot z)\,, \tag{1}$$

with

$K_R = 1.7 \cdot 10^{-14}$ m^2 and

$$a = \begin{cases} a_1 & ,\mathrm{abs}(x) \le x_1 \\ a_1 - \left(\frac{\mathrm{abs}(x)-x_1}{x_2-x_1}\right)a_2 & ,x_1 \le \mathrm{abs}(x) \le x_2 \\ a_1 - a_2 & ,x_2 \le \mathrm{abs}(x) \end{cases},$$

$$b = \begin{cases} 1 & ,\mathrm{abs}(x) \le x_1 \\ 1 - \left(\frac{\mathrm{abs}(x)-x_1}{x_3-x_1}\right)(1-b_3) & ,x_1 \le \mathrm{abs}(x) \le x_3 \\ b_3 & ,x_3 \le \mathrm{abs}(x) \end{cases},$$

$a_1 = 0.0012$, $a_2 = 0.5 \cdot a_1$, $b_3 = 0.05$, $x_1 = 600$ m, $x_2 = 2{,}000$ m, and $x_3 = 5{,}000$ m.

Parameter a is a function of distance x to the ridge axis and describes the depth-dependence of permeability. The almost vertical isotherms that define the edges of the hot slot (see Fig. 1a) require intensive hydrothermal cooling in this region. This is achieved by increasing permeability adjacent to the hot slot using parameter a_2. Beyond a distance of 5 km to the ridge, permeability is reduced by the factor b_3 to avoid high-temperature off-axis venting, which is not observed. It is also required to produce the horizontal isotherms off-axis, which are a key feature in the seismically inferred thermal

structure (see Fig. 1a). The reference permeability K_R has a major control on the axial depth of the melt lens, that is, the depth of the 1,200 ˚C isotherm. The above value leads to a stable melt lens at 1,400 m depth. The shallowest part of the young oceanic crust is likely to be more permeable owing to the presence of a less compact layer of pillow basalts. We account for a 250–m–thick pillow basalt layer[23] by increasing permeability within this depth range using

$$K = K + (K_0 - K) \cdot \exp(d \cdot (z / 250)) , \quad (2)$$

with K_0 = 10^{-13} m^2 and d = -8. K_0 is the permeability at the seafloor and parameter d prescribes the permeability increase with depth within the pillow lavas.

Governing equations of the 3D model. Identical to the 2D model, we assume the convecting fluid to be pure water flowing through a rigid porous medium. Indices f and r in the following equations refer to fluid and rock properties, respectively. Mass transport is described by Darcy's law

$$\boldsymbol{v} = -\frac{K}{\mu_f}\left(\nabla p - \rho_f \boldsymbol{g}\right) , \quad (3)$$

where $\boldsymbol{v}$ is the Darcy velocity, K is permeability (see Extended Data Fig. 1), μ_f is the fluid's dynamic viscosity, ρ_f is the fluid's density, p is pressure, and $\boldsymbol{g}$ is the gravitational acceleration vector. The equation for pressure is derived assuming that the compressibility of the rock is orders of magnitude lower than that of the single-phase fluid, hence negligible. The mass balance is expressed by

$$\phi \frac{\partial \rho_f}{\partial t} = -\nabla \cdot \left(\boldsymbol{v} \rho_f\right) , \quad (4)$$

with ϕ being the porosity of the rock. Substituting equation (3) into equation (4) and noting that the fluid's density is a function of temperature T and pressure yields

$$\phi\rho_f\left(\beta_f\frac{\partial p}{\partial t}-\alpha_f\frac{\partial T}{\partial t}\right)=\nabla\cdot\left(\rho_f\frac{K}{\mu_f}\left(\nabla p-\rho_f\boldsymbol{g}\right)\right), \quad (5)$$

where α_f and β_f are the fluid's thermal expansivity and compressibility, respectively. We solve equation (5) to obtain the pressure field. Hydrostatic pressure at EPR is above the critical point of water (22.1 MPa) so that the fluid is in the supercritical single-phase regime. This allows to express energy conservation using a temperature formulation:

$$\left(\phi\rho_f c_{pf}+(1-\phi)\rho_r c_{pr}\right)\frac{\partial T}{\partial t}=\nabla\cdot\left(k_r\nabla T\right)-\rho_f c_{pf}\boldsymbol{v}\cdot\nabla T+\frac{\mu_f}{K}\boldsymbol{v}^2-\left(\frac{\partial\ln\rho}{\partial\ln T}\right)_p\frac{Dp}{Dt}+Q\ , \quad (6)$$

with c_p being heat capacity, k_r the thermal conductivity of the rock and Q heat sources. Fluid and rock are assumed to be in local thermal equilibrium (that is, $T = T_r = T_f$) so that the mixture appears on the left-hand-side of equation (6). Changes in temperature depend on heat conduction (first term on right-hand-side), heat advection by fluid flow (second term), heat generation by internal friction of the fluid (third term; viscous dissipation; see, for example, page 374 of ref. 39), the pressure-volume work of the fluid (fourth term, see page 337 of ref. 40) and heat generation by crustal accretion processes (fifth term). The latter includes latent heat of crystallization and heat input from magma injection; we obtain both from the 2D model results. All fluid properties (α_f, β_f, ρ_f, μ_f, c_{pf}) are functions of both pressure and temperature. They are evaluated from the same look-up tables used by the 2D code. In both 2D and 3D models we have used the following rock properties: mantle density 3,300 kg m^{-3}, crustal density 2,900 kg m^{-3}, porosity 2%, thermal conductivity 2.5 W m^{-1} K^{-1} and specific heat 1,100 J kg^{-1} K^{-1}. Permeability is calculated using equations (1) and (2); see also Extended Data Fig. 1.

Initial and boundary conditions of the 3D model. Hydrothermal flow is limited to regions below 800 ˚C owing to the permeability decrease at the brittle–ductile transition. Therefore, the 3D model domain is constructed using a bottom isotherm

obtained from the steady overall crustal temperature field from the 2D results. Although hydrothermal flow vanishes towards 800 ˚C (see Fig. 2b) we decided to use the 1,000 ˚C rather than 800 ˚C isotherm to construct the 3D domain. This choice leads to a conductive boundary layer at the base of the 3D domain whose thickness is controlled by how efficiently heat is transported by the fluid flow. The lateral extensions of the 3D domain are chosen such that three-dimensional flow patterns are free to evolve without being strongly affected by the domain sidewalls. We model 6 km of ridge axis, which enables the on-axis vent fields to form at natural spacing of 500–1,000 m. The across-ridge extension is 8 km on both sides of the ridge axis—a choice that is based on the 2D results, where 8 km is the maximum distance at which fluids infiltrate the crust and migrate towards the ridge axis (see Fig. 1b). Fluids intruding further off-axis do not reach the ridge axis but feed diffusive low-temperature venting at greater distances. One reason for this flow pattern is that the best-matching permeability field requires a decrease beyond a distance of 5 km from the ridge axis (see equation (1) and Extended Data Fig. 1). This reduces fluid flow beyond this distance and has fortunate consequences for the 3D model in that the vertical boundaries at 8 km distance have practically no influence on the hydrothermal convection closer to the ridge axis. We account for potential bathymetrical effects on vent field location[41] by using a smoothed (averaged in along-ridge direction) bathymetry of the EPR at 9° N as top boundary. However, the bathymetry in this region is very gentle, with the spreading axis standing about 250 m higher than the sea floor at 8 km distance from the ridge axis. Although computationally it was very challenging, we decided to not enforce symmetry at the ridge axis but to extend the 3D model to both sides of the ridge axis. This allows evolving vent fields to shift across the ridge axis when the feeding plumes interact with each other. All domain boundaries are impermeable except the top boundary, through which

fluids are allowed to enter and leave the domain. All side boundaries are insulating. Since the bottom boundary follows the 1,000 ˚C isotherm obtained from the 2D model, temperature is fixed to this value. At the top boundary we use mixed boundary conditions: temperature is set to a seawater temperature of 2 ˚C where fluids enter the domain, and at locations where fluids leave the domain the vertical temperature gradient is set to zero $\left(\frac{\partial T}{\partial z}=0\right)$ to allow for free venting conditions. All 3D calculations start with cold crustal conditions except near the bottom boundary, where we assume conductive heating over 300 years before model initiation. Thus a smooth, physically meaningful, thermal boundary layer of known thickness exists along the domain bottom at model initiation. We prefer this initial condition over a step function (that is, no conductive heating before model initiation) that instead would lead to a boundary layer whose thickness is controlled by node spacing near the bottom boundary. After model initiation, the thickness of the conductive layer is solely controlled by the 3D fluid flow and the brittle–ductile transition. All 3D calculations ran for 2,000–8,000 years until vent field locations did not change significantly and discharging mass flux became nearly constant. Each calculation required about 3 weeks of calculation time and was conducted on 32 processors.

Numerical techniques in the 3D model. We solve for velocity (equation (3)), pressure (equation (5)) and temperature (equation (6)) separately. Using an implicit finite-element method operating on an unstructured mesh of about 25 million linear-order (4-node) tetrahedral elements, we solve equation (5) to derive the pressure field and subsequently equation (3) to obtain the Darcy velocities. Equation (6) is solved by operator splitting: the advection term is treated by a semi-Lagrange scheme with second-order accurate predictor–corrector integration along flow trajectories and a cubic-order interpolation scheme on the unstructured mesh. All other terms in equation

(6) are also solved using an implicit finite-element method. All matrix equations are solved using preconditioned conjugate gradient algorithms. The choice of preconditoner depends on the equation at hand: for velocity (equation (3)) we use a Jacobi preconditioner (diagonal scaling), and a zero-infill Cholesky factorization is used for the temperature equation (equation (6)). The pressure equation (equation (5)) is the most challenging system of equations to be solved and requires a more advanced technique. Here we use a single V-cycle of geometric multigrid as preconditioner. Jacobi smoothers are used on all multigrid levels except for the coarsest one, where a SuiteSparse[35] Cholesky direct solver is placed. This algorithm is based on developments by ref. 31 in the framework of solving Stokes flow problems. The domain is divided into 32 non-overlapping subdomains (see ExtendedData Fig. 2), each of which associated with one processor of the computing cluster. Solving the above matrix equations essentially requires matrix vector operations, with the Cholesky direct solver on the coarsest multigrid level being the only exception. Hence, after each algebraic operation, partial solutions of subdomains can be corrected at subdomain boundaries to immediately derive a global (that is, domain) solution, which has advantages regarding load balancing between the processors. For more details on the parallelization technique, see ref. 31. The entire 3D model is written in MATLAB and parallelized in MPI-style using MATLAB's Parallel Toolbox.

Data source for EPR vent temperatures. The histogram in Fig. 3 shows a total of 163 *in situ* measurements. We used the following data sets: 24 measurements[42] at EPR 9°–10° N, 83 measurements[43] at EPR 9°–10° N, 40 measurements[44] at EPR 9° 50.3' N, 7 measurements[45] at EPR 17°–18° S, and 9 measurements[46] at EPR 21° 33.7' S.

32. Bauer, O. PROperties of Water and STeam (PROST) version 4.1,

http://fluidos.etsii.upm.es/faculty/Jaime_Carpio/Fumatas_negas/PROST Properties of Water and Steam.htm.

33. Dabrowski, M., Krotkiewski, M. & Schmid, D. W. MILAMIN: MATLAB-based finite element method solver for large problems. *Geochem. Geophy. Geosyst.* **9,** Q04030 (2008).

34. Zienkiewicz, O. C. & Taylor, R. L. *The Finite Element Method*. (Butterworth-Heinemann, 2000).

35. Davis, T. A. & Hager, W. W. Dynamic supernodes in sparse Cholesky update/downdate and triangular solves. *ACM Trans. Math. Softw.* **35**, 27, http://dx.doi.org/10.1145/1462173.1462176 (2009) .

36. Phipps Morgan, J. & Chen, Y. J. The genesis of oceanic crust: magma injection, hydrothermal circulation, and crustal flow. *J. Geophys. Res.* **98,** 6283–6297 (1993).

37. Quick, J. E. & Denlinger, R. P. Ductile deformation and the origin of layered gabbro in ophiolites. *J. Geophys. Res.* **98,** 14015–14027 (1993).

38. Shewchuk, J. R. Delaunay refinement algorithms for triangular mesh generation. *Comput. Geom. Theor. and Appl.* **22,** 21–74 (2002).

39. Magyari, E., Rees, D. A. S. & Keller, B. in *Handbook of Porous Media* (ed. Vafai, K.) 373–406 (Taylor & Francis, 2005).

40. Bird, R. B., Stewart, W. E. & Lightfoot, E. N. *Transport Phenomena*. (Wiley, 2007).

41. Bani-Hassan, N., Iyer, K., Rüpke, L. H. & Borgia, A. Controls of bathymetric relief on hydrothermal fluid flow at mid-ocean ridges. *Geochem. Geophy. Geosyst.* **13,** Q05002 (2012).

42. Von Damm, K. L. Chemistry of hydrothermal vent fluids from 9°–10° N, East Pacific Rise: 'time zero,' the immediate posteruptive period. *J. Geophys. Res.* **105,** 11203–11222 (2000).

43. Shanks, W. C. Stable isotopes in seafloor hydrothermal systems: vent fluids, hydrothermal deposits, hydrothermal alteration, and microbial processes. *Rev. Mineral. Geochem.* **43,** 469–525 (2001).

44. Von Damm, K. L. in *Mid-Ocean Ridges: Hydrothermal Interactions Between the Lithosphere and Oceans* (eds German, C. R., Lin, J. & Parson, L.) **148,** 285–304 (American Geophysical Union, 2004).

45. Charlou, J. L. *et al.* Mineral and gas chemistry of hydrothermal fluids on an ultrafast spreading ridge: East Pacific Rise, 17° to 19°S (Naudur cruise, 1993) phase separation processes controlled by volcanic and tectonic activity. *J. Geophys. Res.* **101,** 15899–15919 (1996).

46. Von Damm, K. L. *et al.* Extraordinary phase separation and segregation in vent fluids from the southern East Pacific Rise. *Earth Planet. Sci. Lett.* **206,** 365–378 (2003).

Figure 1

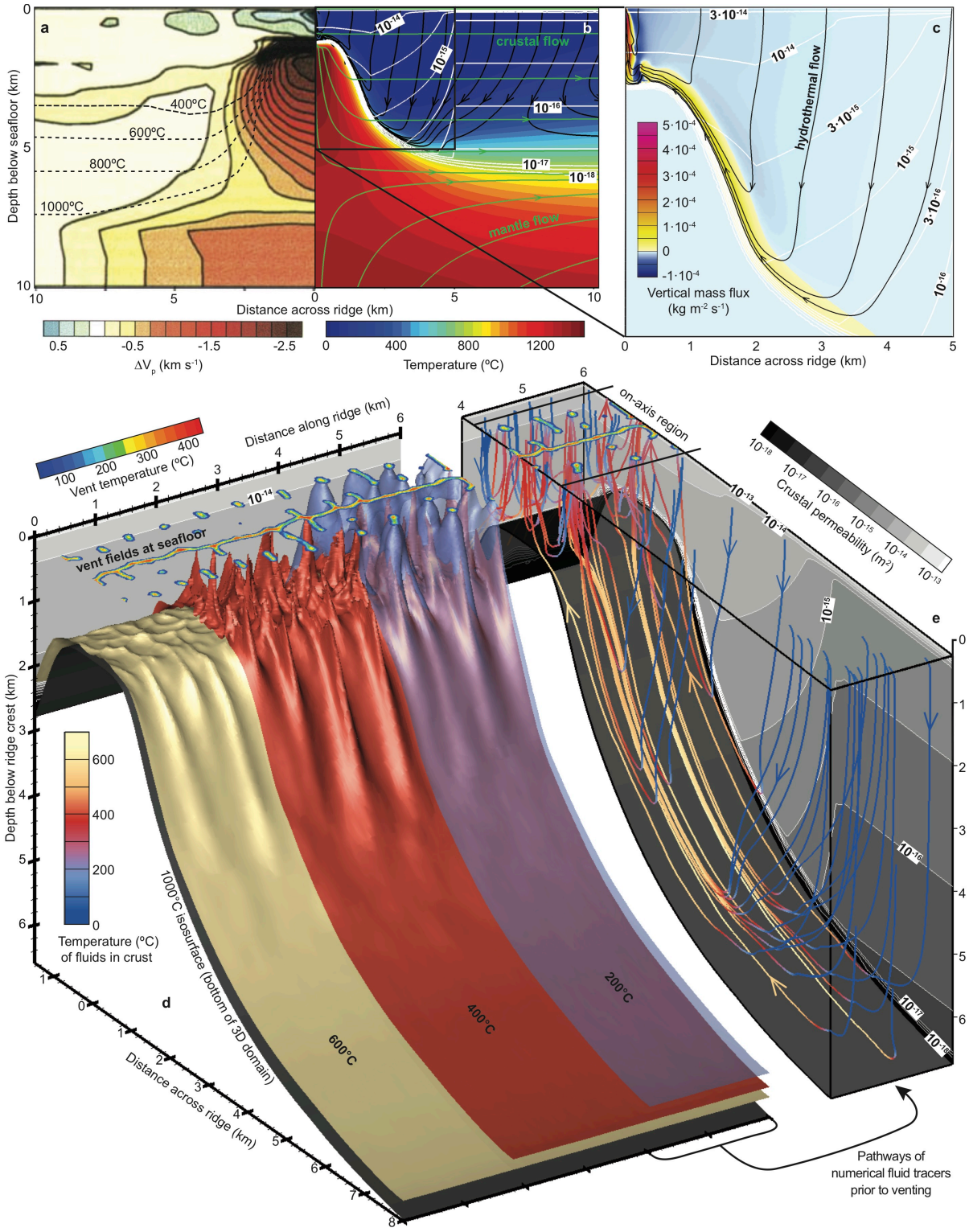
a
b
c
d
e
400°C
600°C
800°C
1000°C
crustal flow
mantle flow
hydrothermal flow
Depth below seafloor (km)
Distance across ridge (km)
ΔV_p (km s⁻¹)
Temperature (°C)
Vertical mass flux (kg m⁻² s⁻¹)
Vent temperature (°C)
Distance along ridge (km)
vent fields at seafloor
on-axis region
Crustal permeability (m²)
Depth below ridge crest (km)
Temperature (°C) of fluids in crust
1000°C isosurface (bottom of 3D domain)
Distance across ridge (km)
200°C
400°C
600°C
Pathways of numerical fluid tracers prior to venting

Figure 2

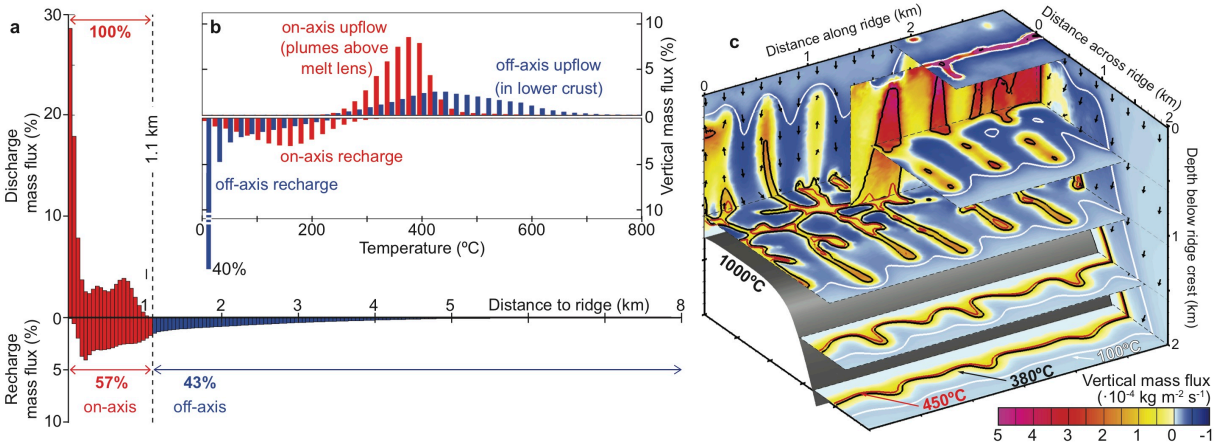
a
100%
1.1 km
Discharge mass flux (%)
Recharge mass flux (%)
57%
on-axis
43%
off-axis
Distance to ridge (km)
b
on-axis upflow
(plumes above
melt lens)
off-axis upflow
(in lower crust)
on-axis recharge
off-axis recharge
40%
Temperature (ºC)
Vertical mass flux (%)
c
Distance along ridge (km)
Distance across ridge (km)
Depth below ridge crest (km)
1000°C
380°C
450°C
100°C
Vertical mass flux
(·10⁻⁴ kg m⁻² s⁻¹)

Figure 3

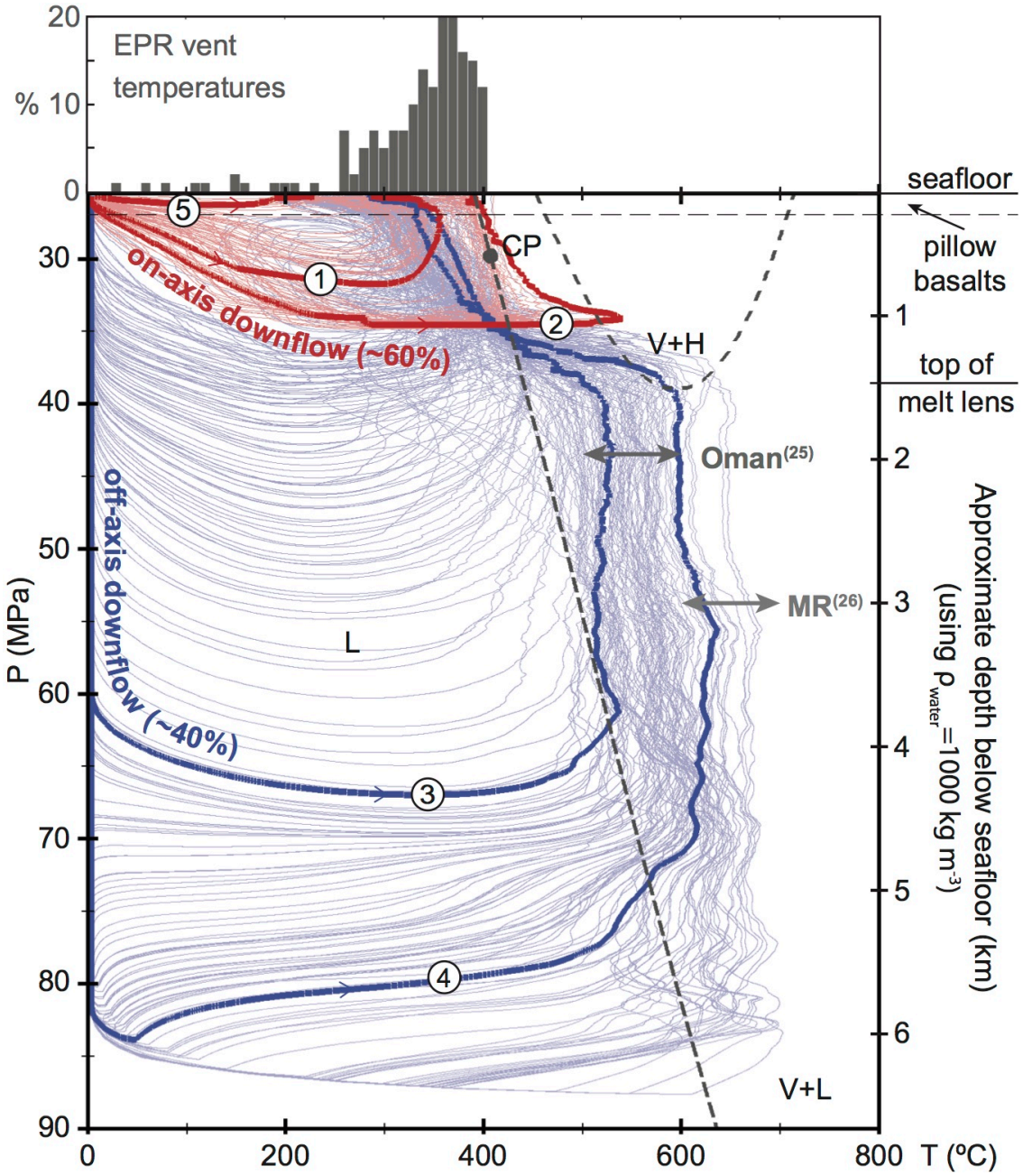
EPR vent temperatures
20
% 10
0
seafloor
pillow basalts
top of melt lens
CP
V+H
Oman(25)
MR(26)
L
V+L
on-axis downflow (~60%)
off-axis downflow (~40%)
1
2
3
4
5
P (MPa)
30
40
50
60
70
80
90
0
200
400
600
800
T (°C)
1
2
3
4
5
6
Approximate depth below seafloor (km)
(using ρwater=1000 kg m-3)

Extended Data Figure 1

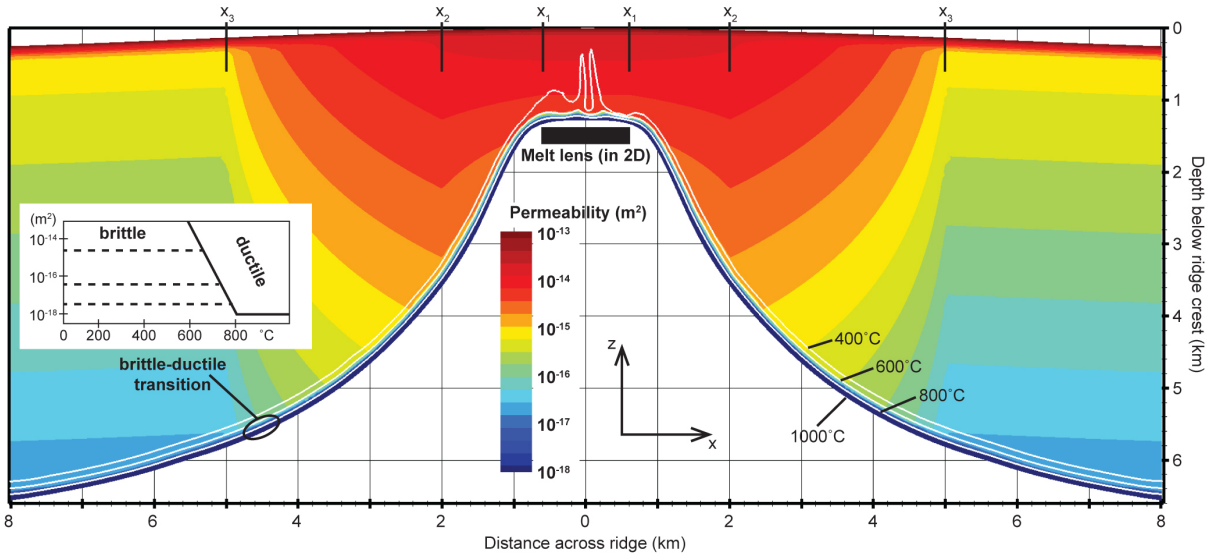

Extended Data Figure 2

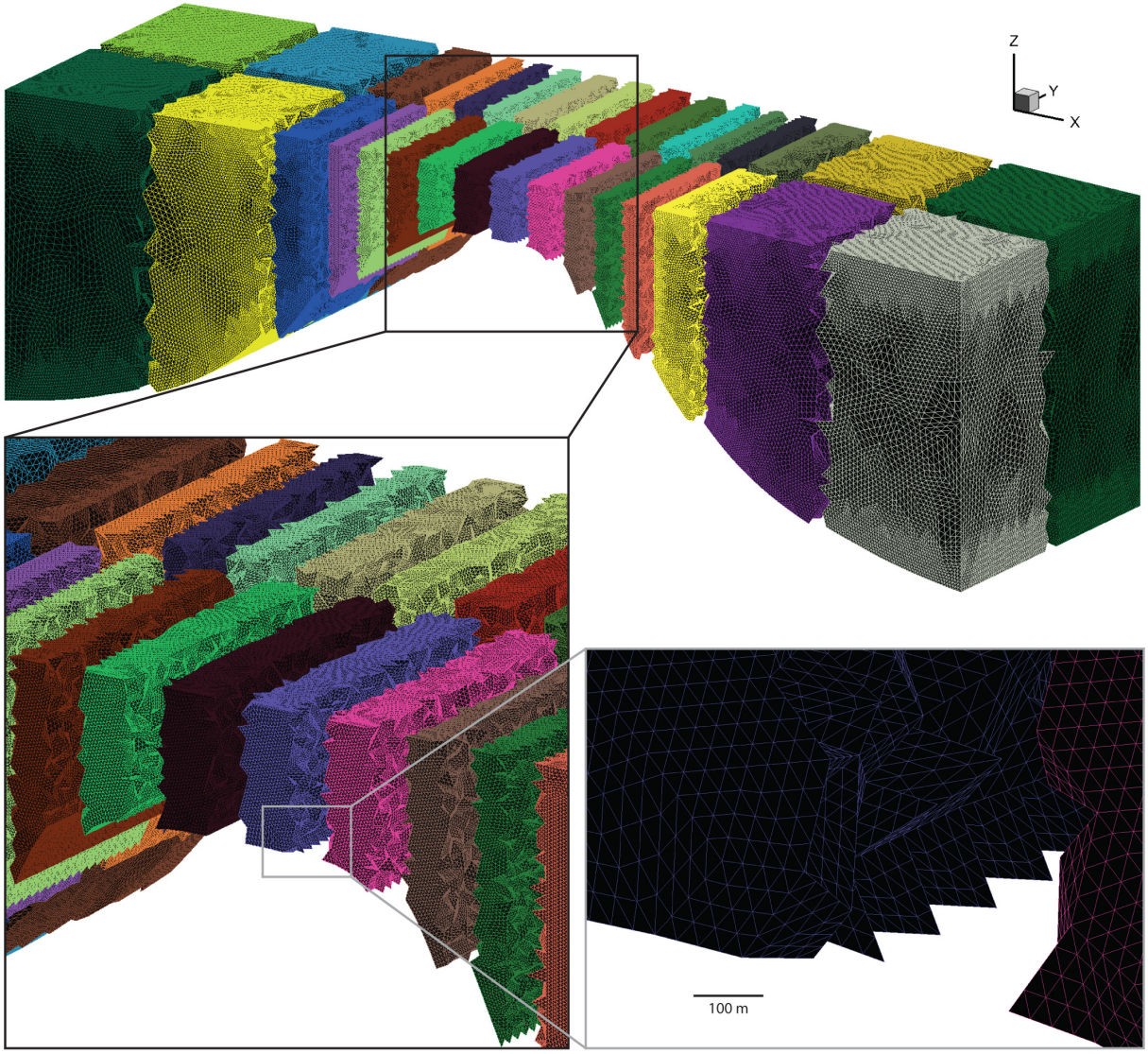

Extended Data Figure 3

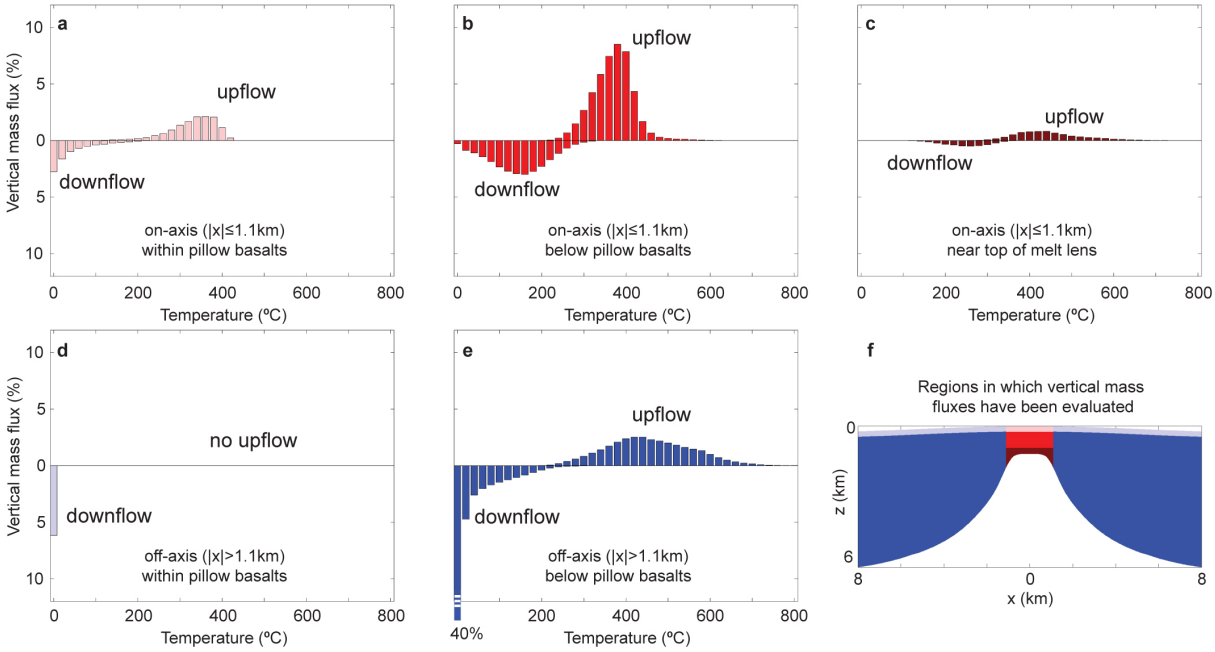

Extended Data Figure 4

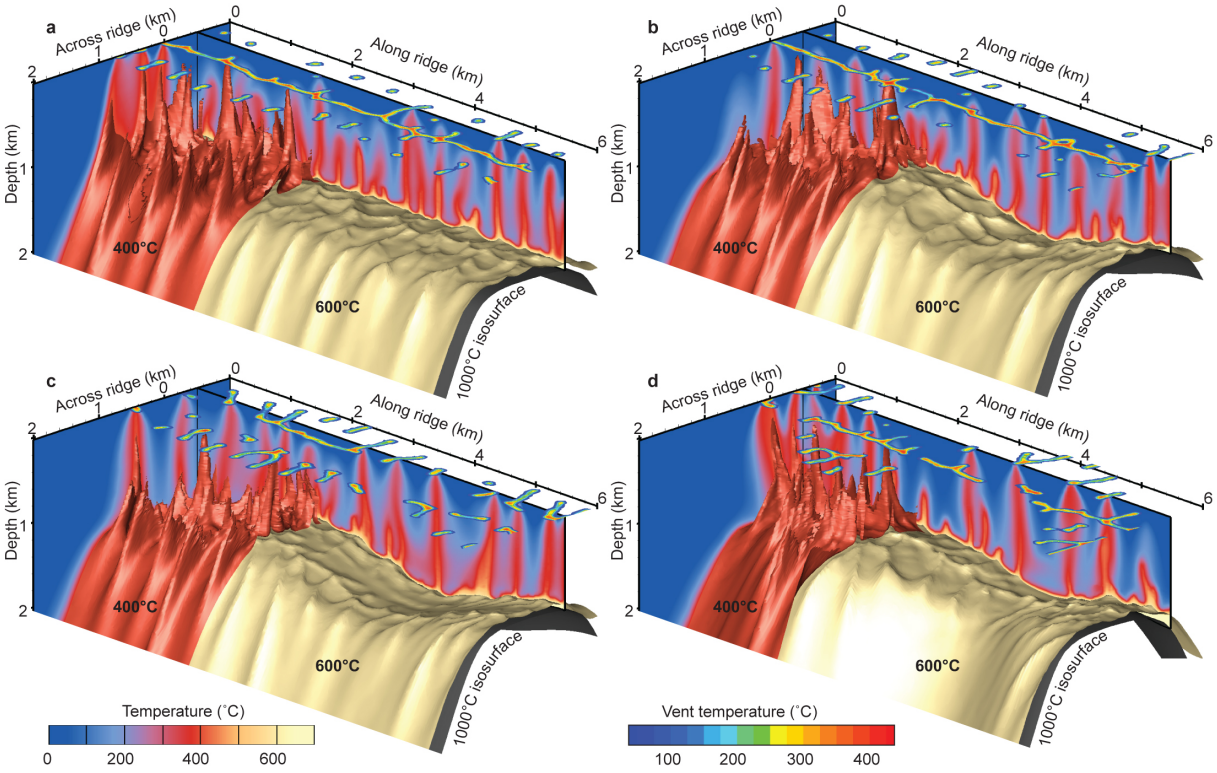

Extended Data Figure 5